An et al. *NPG Asia Materials* (2021) 13:69
https://doi.org/10.1038/s41427-021-00335-7

NPG Asia Materials

ARTICLE Open Access

Experimental realization of strain-induced room-temperature ferroelectricity in $SrMnO_3$ films via selective oxygen annealing

Hyunji An[1], Young-Gyun Choi[1], Yong-Ryun Jo[1], Hyo Jin Hong[1], Jeong-Kyu Kim[2], Owoong Kwon[3], Sangmo Kim[4], Myungwoo Son[1], Jiwoong Yang[1], Jun-Cheol Park[1], Hojoong Choi[1], Jongmin Lee[1], Jaesun Song[1], Moon-Ho Ham[1], Sangwoo Ryu[5], Yunseok Kim[3], Chung Wung Bark[4], Kyung-Tae Ko[2,6], Bong-Joong Kim[1] and Sanghan Lee[1]

Abstract

Antiferromagnetic-paraelectric $SrMnO_3$ (SMO) has aroused interest because of the theoretical strong coupling between the ferroelectric and ferromagnetic states with increasing epitaxial strain. In strained SMO films, the <110> polarized state and polar distortions have been observed, although high leakage currents and air degradation have limited their experimental verification. We herein provide a conclusive demonstration of room-temperature ferroelectricity and a high dielectric constant ($\varepsilon_r = 138.1$) in tensile-strained SMO by securing samples with insulating properties and clean surfaces using selective oxygen annealing. Furthermore, a paraelectricity and low dielectric constant ($\varepsilon_r = 6.7$) in the strain-relaxed SMO film have been identified as properties of the bulk SMO, which directly proves that the ferroelectricity of the tensile-strained SMO film is due to strain-induced polarization. We believe that these findings not only provide a cornerstone for exploring the physical properties of multiferroic SMO but also inspire new directions for single-phase multiferroics.

Introduction

Multiferroic materials exhibiting simultaneous ferroelectric and ferromagnetic properties have attracted much attention over the last decades as promising candidates for next-generation devices such as multiple-state memory elements, electrical-field-controlled ferromagnetic resonance devices, and transducers with magnetically modulated piezoelectricity[1,2]. In essence, ferroelectricity prefers the d^0-ness configuration for transition metal off-centering in a perovskite structure, whereas magnetism stems from uncompensated spin magnetic moments of the occupied d electrons[3,4]. Owing to competing requirements, multiferroicity with strong properties has been difficult to implement. Since Kimura demonstrated multiferroicity in $TbMnO_3$[5,6], significant progress has been made such that multiferroic systems can be classified into types I and II[7,8]. In type-I systems, an electric field can drive changes in the magnetization, although a rather weak coupling between ferroelectricity and magnetism was observed because ferroelectricity and magnetic order originate from two different cations[9]. Conversely, type-II multiferroics exhibit very strong magnetoelectric couplings because the magnetic order breaks the inversion symmetry of the material and induces a ferroelectric phase; however, their spontaneous polarization is generally small (~10^{-2} μC/cm^2). Due to these limitations of conventional multiferroics, a new multiferroic system is urgently needed for practical device applications[10].

$SrMnO_3$ (SMO) goes beyond the standard paradigm of type I/type II multiferroics because both ferroelectric and ferromagnetic properties are primary order parameters that in principle emerge independent of each other but

Correspondence: Sanghan Lee (sanghan@gist.ac.kr)
[1]School of Materials Science and Engineering, Gwangju Institute of Science and Technology, Gwangju 61005, Republic of Korea
[2]Max Planck POSTECH/Hsinchu Center for Complex Phase Materials & Department of Physics, POSTECH, Pohang 37673, Republic of Korea
Full list of author information is available at the end of the article

are nevertheless strongly coupled[11]. Recent theoretical studies have reported that the bulk antiferromagnetic-paraelectric ground state in some perovskites is driven to a new multiferroic state by increasing the epitaxial strain[12–15]. This multiferroic phase emerges from a strong interaction between the spin order and the lattice phonons (so-called "spin-phonon coupling") when the unit cell volume is increased[16]. Strain-induced multiferroicity based on spin-phonon coupling was first experimentally demonstrated in the $EuTiO_3$ of A-site rare-earth systems[16,17]; however, weak magnetoelectric coupling was also observed because ferroelectricity and magnetism originated from different lattice sites[16]. For this reason, the SMO of a B-site magnetic system was of particular interest. In this material, strong magnetoelectric couplings were expected since the off-centered Mn^{4+} ($3d^3$) ion carries both electric and spin magnetic moments[15,18].

According to density functional theory (DFT) calculations, an epitaxial SMO film generates ferroelectric polarization in the <110> direction at epitaxial tensile strains above 1%, whereas high tensile strains above 4.5% are required for ferromagnetism[15]. Because of the difficulty of implementing high strain states, experimental studies related to strain-induced ferroelectricity preceded those of ferromagnetism. In particular, Becher and Guzman et al. fabricated epitaxial 1.7% tensile-strained SMO thin films with thicknesses of 10−20 nm using the $(LaAlO_3)_{0.3}(Sr_2TaAlO_6)_{0.7}$ (LSAT) substrate. They confirmed its <110> polarized state and polar distortions by second harmonic generation (SHG) and scanning transmission electron microscopy (STEM)[19,20]. However, high leakage currents and the presence of oxygen vacancies were also observed[19,20]. More recently, surface and internal cracks in SMO thin films were found under strained states[9,21,22]. These reports revealed that the strained SMO film could easily degrade in air so that cracks appeared due to partial epitaxial stress relief. Air degradation is an important challenge in the SMO research field, as the intrinsic properties of thin films deteriorate due to chemical or mechanical instability when the thin film is exposed to air, consequently reducing the device performance[23–25]. These issues make it difficult to directly investigate the intrinsic ferroelectric and dielectric properties[26], thus hampering the experimental verification of strain-induced SMO thin films. Furthermore, in-depth studies analyzing and solving high leakage current and air degradation issues have not been reported.

Herein, we propose a selective oxygen annealing (SOA) method as an innovative strategy to effectively suppress the leakage current while protecting strained SMO films from air degradation. Because SOA imparts insulating properties and suppresses surface crack issues, the intrinsic room-temperature ferroelectricity of tensile-strained SMO thin films can be demonstrated for the first time, and their dielectric properties can be investigated. We fabricated a 1.7% tensile-strained SMO thin film with a thickness of 20 nm on an LSAT substrate utilizing pulsed laser deposition (PLD) and fabricated films with various thicknesses (45, 69, 92, and 115 nm) to systematically control the degree of strain. The samples were then postprocessed using the SOA method. Compared with the semiconductor properties (current density > 10 A/cm^2 and dielectric loss (tan δ) > 10) of the as-grown films, the SOA-treated SMO films exhibited insulating properties (current density < 10^{-5} A/cm^2 and tan δ < 0.1). Based on these insulating properties, 1.7% tensile-strained SMO films with a polarization hysteresis loop ($P_s = 1$ μC/cm^2) and a high dielectric constant ($\varepsilon_r =$ 138.1) were demonstrated at room temperature for the first time. Furthermore, the strain-induced ferroelectricity of SMO was verified by examining the significant changes in the polarization hysteresis loops and dielectric constants as the epitaxial strain increased.

Materials and methods

Sample preparation

The $SrMnO_3$ ceramic was synthesized using a solid-state reaction method with the following starting binary oxide powders as raw materials: $SrCO_3$ (99.9%, Kojundo Chemical Lab.) and $MnCO_3$ (99.9%, Kojundo Chemical Lab.). Based on the ceramic target, 1.7% tensile-strained $SrMnO_3$ (SMO) thin films ($a_{cubic} = 0.3805$ nm) were grown on LSAT (001) substrates ($a_{cubic} = 0.3869$ nm). SMO thin films with thicknesses of 20, 45, 69, 92, and 115 nm were fabricated at a high temperature of 900 °C, oxygen pressure of 200 mTorr, and laser fluence of 1 J/cm^2 using PLD (KrF, $\lambda = 248$ nm). To perform SOA, we additionally grew $SrRuO_3$ layers ($a_{cubic} = 0.3926$ nm) on the as-grown SMO films at a temperature of 750 °C, oxygen pressure of 100 mTorr, and laser fluence of 2 J/cm^2 using PLD. In a tube furnace, the $SrRuO_3$ (SRO)-capped SMO films were annealed under a high-purity oxygen (99.995%, Sinil gas) atmosphere at a temperature of 600 °C with an oxygen flow rate of 1.5 L/min in atmospheric pressure for 2 h. Finally, the SRO capping layer was selectively etched in a sodium metaperiodate ($NaIO_4$) etchant.

Thin film characterizations

The structural properties were analyzed via XRD (D8 Advance, Bruker) using Cu Kα radiation ($\lambda = 1.5418$ Å). Reciprocal space mapping (RSM) was performed using the 3 A beamline at the Pohang Light Source with a six-circle Paul Scherrer Institute (PSI) diffractometer. Surface morphologies were observed using a standard optical microscope with a CCD camera and an atomic force microscope (Park Systems NX10). Atomic-scale structural characteristics and elemental mapping were investigated

using a high-resolution transmission electron microscope (TecnaiTM G2 F30 S-Twin, 300 KeV, FEI). SRO interdigitated electrodes (IDEs) were patterned on the surface using a lift-off technique to minimize damage to the surface. The finger length ($L = 1000$ μm), finger width ($w = 6$ μm), gap spacing ($g = 6$ μm), and electrode period ($P = 12$ μm) of the IDE pattern were confirmed according to Fig. S1 (Supplementary information). The total number of finger pairs was $N = 30$. The current density J–V curve was investigated under ambient conditions using a semiconductor parameter analyzer (Keithley, 4200-SCS). The dielectric constant and dielectric loss were measured using an LCR meter (Agilent, 4294A). The P–E loop was measured using a ferroelectric analyzer (Precision Multiferroic, Radiant Technologies Inc.).

Results and discussion

Tensile-strained $SrMnO_3$ thin films

Tensile-strained $SrMnO_3$ (SMO) thin films with thicknesses of 20, 45, 69, 92, and 115 nm were grown on an LSAT substrate by PLD. LSAT substrates were used to achieve a nominal in-plane epitaxial strain of +1.7% for the bulk SMO. As shown in Fig. 1a, X-ray diffraction (XRD) θ–2θ patterns revealed that the SMO thin films with a cubic phase were highly (0 0 l)-oriented. The SMO (002) peak of the thinnest SMO film (20 nm) shifted to a higher angle based on the black dotted reference line for the bulk SMO. Additionally, this peak gradually returned toward the reference line as the thickness increased to 115 nm. Moreover, the RSM results confirmed that the in-plane lattice parameters of the thinnest SMO film (20 nm thick) were coherently strained on the LSAT substrate (Fig. 1b), and the tensile strain was relaxed with increasing film thickness (Fig. S2 and Table S1). These XRD results demonstrate that the 20-nm thick SMO thin film was 1.7% tensile-strained by the LSAT substrates; the epitaxial strain was gradually relaxed as the thickness increased from 20 nm to 115 nm. The rocking curves for the SMO (002) reflection were measured to determine the out-of-plane mosaic spread and the crystalline quality. As shown in Fig. 1c–e, the full widths at half maximum (FWHM) of the (002) reflection rocking curves of the SMO thin films with thicknesses of 20 nm, 45 nm, 69 nm, 92 nm, and 115 nm were 0.032°, 0.055°, 0.109°, 0.164°, and 0.227°, respectively. This indicates that the thinnest SMO film has a high out-of-plane crystallinity and that the crystallinity gradually deteriorates as the thickness increases.

Microcracks were identified on the surface of the as-grown SMO films, similar to previous experimental results (Figs. S3a–c)[9,22]. For these films, high leakage currents and dielectric losses were also confirmed by investigating the leakage current density (J) and dielectric loss (tan δ) versus voltage curves, as shown by the dotted lines in Fig. 2e, f. Consequently, both the high leakage current[19] and surface crack[9,22] issues were similarly observed in our as-grown SMO films.

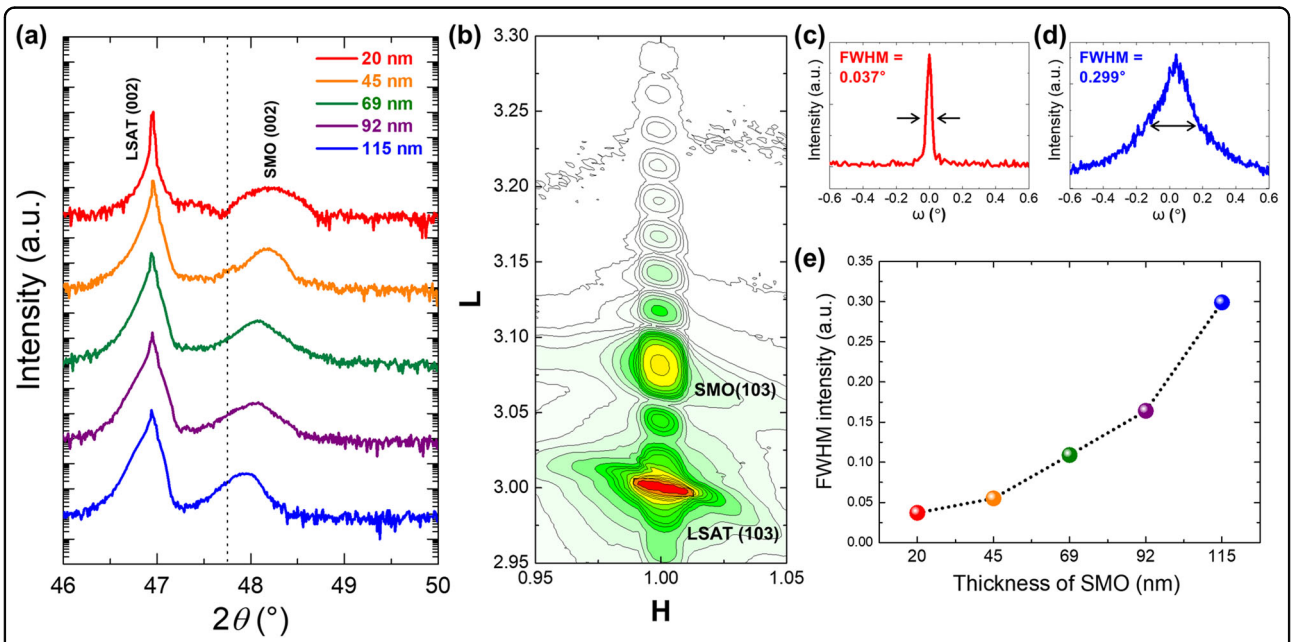

Fig. 1 Tensile-strained $SrMnO_3$ thin films. a XRD θ–2θ patterns of the SMO thin films on the LSAT (001) substrates with thicknesses of 20–115 nm. Cubic SMO (002) in bulk, the reference, is denoted by the black dotted line (JCPDS no.: 23-1413). **b** RSM data for the SMO thin film with a thickness of 20 nm. **c**, **d** Rocking curves and FWHMs for the 20 nm and 115 nm films, respectively. **e** FWHMs of SMO films with various thicknesses (20, 45, 69, 92, and 115 nm).

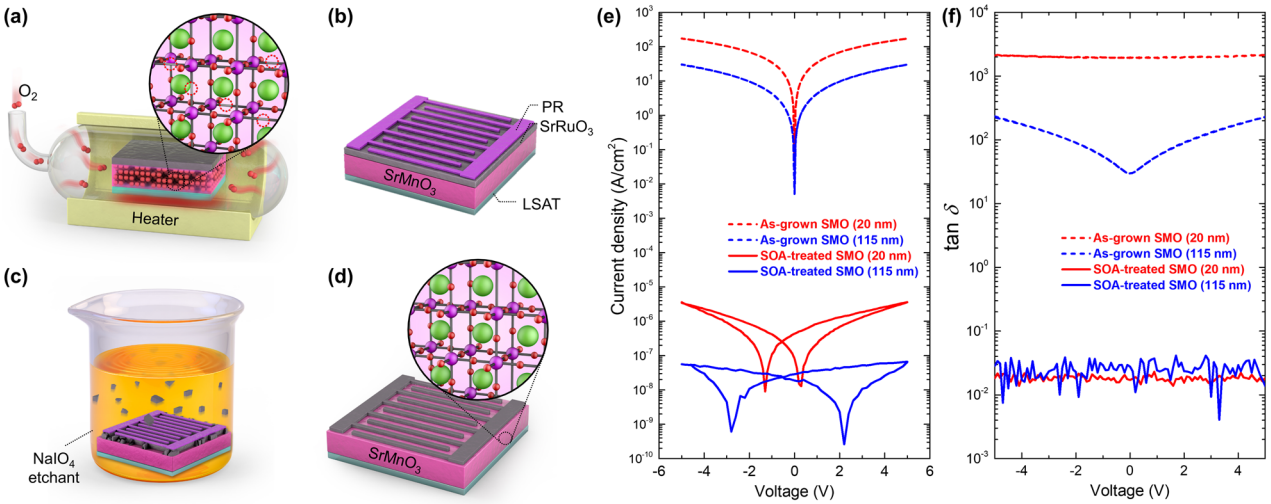

Fig. 2 Selective oxygen annealing method and improved insulating properties. a–d Schematics of the selective oxygen annealing process including the interdigitated electrode (IDE) manufacturing process for the SMO thin films. **a** Tube furnace annealing of the SRO-capped SMO film on LSAT at a high temperature (600 °C) and an oxygen-rich atmosphere (O_2 flow: 1.5 L/min in atmospheric pressure). **b** Typical photolithography process with an interdigitated photoresist (PR) pattern on the sample. **c** Selective etching of SRO on the SMO film using a $NaIO_4$ solution. **d** Patterned SRO IDE on the SMO films after removing the PR pattern using an acetone solution. **e** Current density versus voltage curves and **f** dielectric loss (tan δ) versus voltage curves of the as-grown SMO (applied with processes **b**–**d**) and SOA-treated SMO films (applied with processes **a**–**d**) with thicknesses of 20 and 115 nm.

Selective oxygen annealing

To overcome the high leakage current and air degradation issues, we devised a SOA method. This method entails fabricating epitaxial $SrRuO_3$ (SRO) capping layers (20 nm) on the as-grown SMO thin films and performing ex situ annealing at a temperature of 600 °C under an oxygen-rich atmosphere, followed by removal of the SRO capping layer, as shown in Fig. 2a, c. The overall process, including the interdigitated electrode (IDE) manufacturing process, is illustrated in detail in Fig. 2a−d. The use of a capping layer was recently proposed by several research groups to prevent air degradation of strained SMO thin films[9,22]. Consequently, they confirmed the ferroelectric polarization hysteresis loop for the $DyScO_3$ (DSO)-capped SMO thin film at a low temperature (10 K). However, the ferroelectric hysteresis loops of the DSO-capped SMO thin film may also include the interfacial characteristics of the DSO layer (such as the strain effect) as well as the characteristics of SMO. For a more accurate investigation, we used the SRO capping layer, which can be removed after oxygen annealing, and then the room-temperature ferroelectricity of the single SMO thin films was investigated. The advantages of the SRO capping layer can be summarized as follows: First, coherent growth is expected on SMO films because SRO has the same cubic perovskite structure as SMO, and its larger lattice parameter (a_{cubic} = 0.3926 nm) than SMO (a_{cubic} = 0.3805 nm) can stabilize the films over a large range of strain states[22]. Second, only SRO can be selectively etched by the $NaIO_4$ etching solution[27,28]. Last, SRO can also be used as a top electrode, thus avoiding additional processing for electrical measurements.

After applying the SOA method, we ascertained the purity of the SMO thin film; the complete removal of SRO is shown in Fig. S3 (surface morphological aspect), Fig. S4 (chemical aspect), and Fig. S5 (structural aspect), and significant suppression of the surface crack issues is shown in Fig. S3. Notably, a significant reduction in the leakage current and dielectric loss of the SOA-treated SMO films was observed, as shown by the solid lines in Fig. 2e and f. In these figures, to show the dramatic effect of SOA on the electrical properties, we plotted the J–V and tan δ–V switching curves of both the as-grown SMO films (thickness: 20 nm, 115 nm) and SOA-treated SMO films (thickness: 20 nm, 115 nm). Figure 2e shows that the semiconductor loops of the as-grown SMO films were equally transformed to insulating butterfly loops after SOA, which exhibit typical metal-insulator-metal capacitors[29,30]. The strain-relaxed film (115 nm) has a larger insulating butterfly loop than the fully strained film (20 nm), which indicates the amount of charge trapping by gate bias sweeping[31]. Such a difference between the two films may be attributed to the thickness dependence or the emergence of ferroelectric phases in strain-relaxed films (20 nm). Note that after performing SOA, the leakage current density of the fully strained SMO film (20 nm) was reduced by eight orders of magnitude from 180 A/cm^2 to 3.8×10^{-6} A/cm^2 at 5 V. Similarly, the strain-relaxed SMO

film (115 nm) was also reduced by nine orders of magnitude from 29 A/cm^2 to 6.9 × 10^{-8} A/cm^2 at 5 V. Figure 2f shows that a tan δ of less than 0.1 was found for the SOA-treated SMO films, which was also significantly reduced compared to the high tan δ (10^2–10^3) of the as-grown films. These results revealed that the SOA method can not only significantly suppress the high leakage current of the strained SMO film but also protect the surface from cracks. Moreover, the *J*–*V* resistive switching and low tan δ measured for the SOA-treated SMO films indicate that the samples are suitable for investigating intrinsic ferroelectric and dielectric properties and that they can be applied in a typical capacitor without leakage issues.

Improved crystal structure

To thoroughly verify the SOA effect in reducing the high leakage current, structural analyses of the SMO thin films before and after oxygen annealing were carried out. As shown in Fig. 3a, b, the XRD θ–2θ patterns for the SRO (20 nm)-capped SMO (thickness: 20 nm, 115 nm) films reveal that only the SMO (002) peaks equally shifted to a higher angle without a remarkable change in the SRO (002) peaks after oxygen annealing. As shown in Figs. S6a–c, this peak shift of SMO (002) occurred for all samples. Additional RSM data of both the as-grown SMO and SOA-treated SMO films also demonstrated that a fully strained in-plane lattice parameter of SMO on the LSAT substrate was maintained after oxygen annealing (Fig. S6d, e). Therefore, the peak shift results of SMO indicate that a large amount of oxygen was selectively incorporated into SMO rather than into SRO during SOA so that only the c-lattice parameter of SMO was changed. Based on the XRD data, the *c*-lattice parameters of the as-grown SMO and SOA-treated SMO films were calculated using Bragg's law, as shown in Fig. 3c. The results show that the *c*-lattice parameters of SMO were consistently contracted after SOA. In particular, it was confirmed that the c-lattice parameter of the SOA-treated fully strained SMO thin film (20 nm) was reduced to 3.769 Å compared to the 3.775 Å of the as-grown SMO thin film (20 nm).

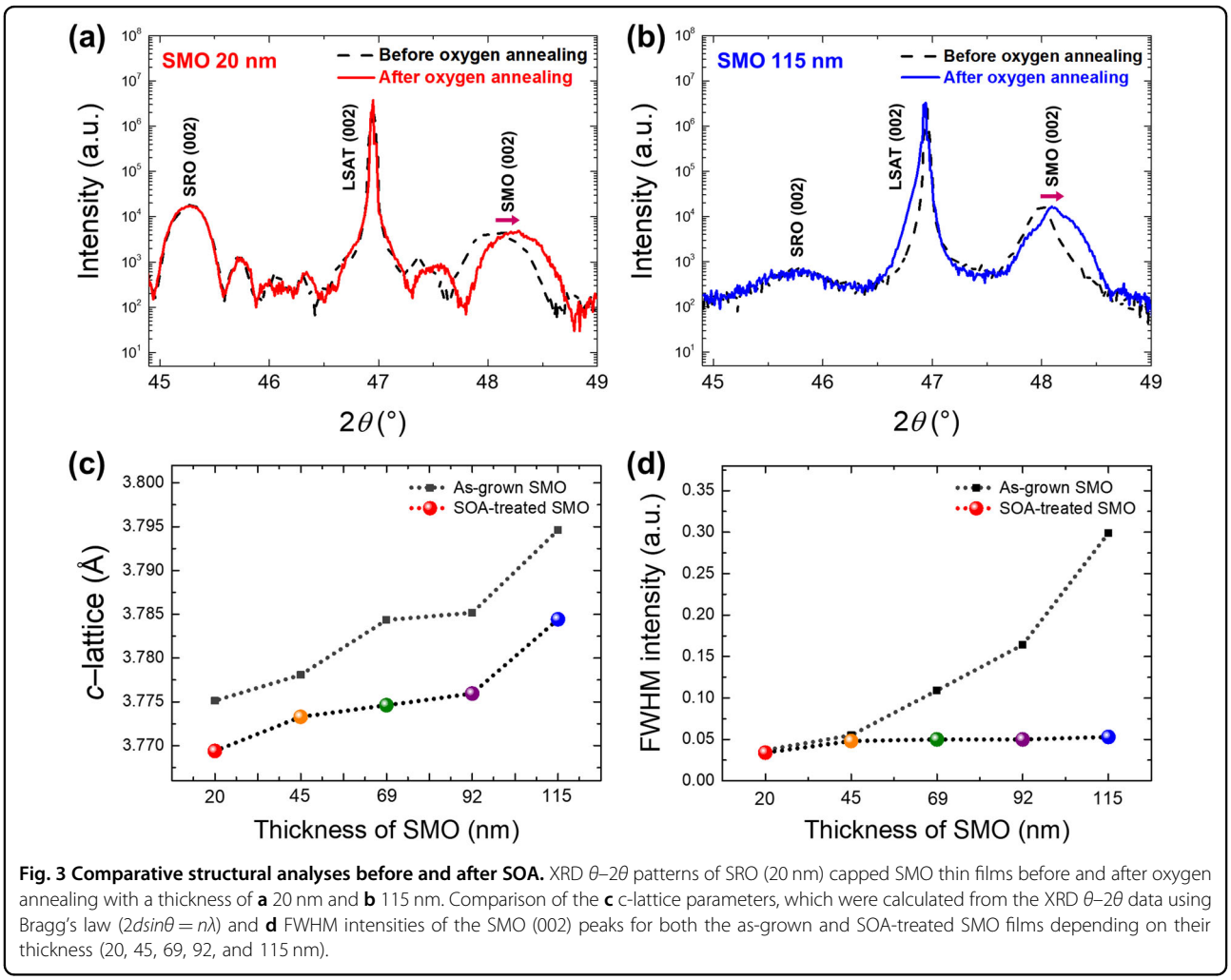

Fig. 3 Comparative structural analyses before and after SOA. XRD θ–2θ patterns of SRO (20 nm) capped SMO thin films before and after oxygen annealing with a thickness of **a** 20 nm and **b** 115 nm. Comparison of the **c** c-lattice parameters, which were calculated from the XRD θ–2θ data using Bragg's law ($2dsin\theta = n\lambda$) and **d** FWHM intensities of the SMO (002) peaks for both the as-grown and SOA-treated SMO films depending on their thickness (20, 45, 69, 92, and 115 nm).

This value is closer to the theoretically expected c-lattice parameter (3.624 Å) of the fully constrained SMO film on the LSAT substrate[9], allowing us to predict that oxygen vacancies are additionally filled by SOA treatment. This c-lattice contraction was also observed in a previous paper of oxygen-annealed $La_{0.84}Sr_{0.16}MnO_{3-\delta}$ (LSMO)[32], which proved that the lattice contraction was due to the increased ratio of Mn^{4+} ions with a smaller ionic radius than Mn^{3+} ions by oxygen incorporation. Moreover, all FWHMs of the SMO (002) peaks were also reduced after SOA, indicating that the crystallinity of the SOA-treated SMO films was improved (Fig. 3d).

Indeed, it is known that the c-axis lattice parameter of strained SMO thin films is elongated due to air degradation[21,22]. This elongation results from structural defects such as surface and internal cracks for epitaxial-strain relief of the strained SMO thin film. Since these structural defects were also observed in our as-grown SMO thin films (Figs. S3a–c), their c-lattice parameters may be more elongated than the genuine lattice parameter. However, compared to the c-lattice parameters of the as-grown films, those of the SOA-treated SMO films were conversely contracted, and furthermore, the film crystallinities were improved for all samples. Therefore, the structural defects of SMO were considerably reduced by suppressing air degradation and incorporating additional oxygen during SOA.

To confirm the effects of the capping layer and oxygen annealing, we also performed oxygen annealing for the as-grown SMO thin films (thickness: 20 nm, 115 nm) without the SRO capping layer. In this case, there were no changes in the *c*-lattice parameter and conductivity of SMO compared to those of the as-grown SMO (Fig. S7). Therefore, in situ SRO capping should follow SMO growth and precede oxygen annealing to achieve the SOA effect. Moreover, the electrical properties of the as-grown SMO, which are SRO-capped SMO thin films without oxygen annealing, exhibited high leakage currents, as shown in Fig. 2e, f. Thus, these results demonstrate that oxygen annealing plays a prominent role in suppressing the leakage current and that the capping layer plays a role in preventing air degradation of the films. Through a comparative analysis of each SOA process, we identified that each process should be performed sequentially; thus, this is the optimized method to effectively suppress both aforementioned issues of SMO. We call this method SOA, which includes both selective oxygen incorporation for SMO and selective etching of the SRO capping layer.

Atomic-scale observation

For atomic-scale structural analysis, we performed a cross-sectional transmission electron microscopy (TEM) analysis of the as-grown SMO and SOA-treated SMO films. The cross-sectional samples were prepared along the <110> polar domain orientation of SMO using a focused ion beam, as depicted schematically in Fig. 4b. Figure 4a and c show the high-resolution TEM (HRTEM) images of the as-grown SMO film (20 nm) and SRO (20 nm)-capped SMO (20 nm) film after oxygen annealing, respectively. The HRTEM image with the corresponding fast Fourier transform (FFT) patterns in Fig. 4a shows that the SMO film is a single crystal with planar defects (i.e., stacking faults)[33], as indicated by the streaks along the (001) direction of the SMO FFT pattern (upper inset of Fig. 4a).

In contrast, the HRTEM image of the SRO (20 nm)-capped SMO (20 nm) film on the LSAT substrate after oxygen annealing (Fig. 4c) shows that the SRO is a single crystal and grows epitaxially on the SMO without observable defects, as the selective area diffraction (SAD) pattern of the three layers in Fig. 4d presents discrete diffraction spots with no streaks, in contrast to the pattern from the SMO layer in Fig. 4a. Specifically, it was found that the (001) lattice spacings of the three layers are 3.805 Å (SMO), 3.868 Å (LSAT) and 3.926 Å (SRO), while those of the (110) lattice of the three layers are the same. Furthermore, the HRTEM image (Fig. 4e) taken from the boxed area in Fig. 4c shows off-centering of the Mn cations (Δx: 96 pm) along the [110] direction from the intrinsic centrosymmetric positions, which is consistent with the polar distortions previously identified in the strained SMO thin films on LSAT[19,20]. We presume that such crystallinity with no large-scale defects in the SMO layer is attributed to the SOA process. Thus, the SMO thin film exhibited insulating properties with no defect-driven leakage current.

Strain-induced ferroelectricity

To confirm strain-induced ferroelectricity, we measured the polarization hysteresis loops (P–E loops) and dielectric constant (ε_r)–V curves for the SOA-treated SMO films with various thicknesses. Based on the verified insulating properties (Fig. 2e, f), the SOA-treated SMO films with thicknesses of 20, 45, 69, 92, and 115 nm were found to exhibit polarization hysteresis loops at room temperature, as shown in Fig. 5a. The P–E loop shapes of the 69, 92, 115 nm thick films are close to the linear capacitor, and the 20 nm and 45 nm thick films are similar to the ferroelectric capacitor[34]. As the SMO thickness decreased, it was confirmed that the change in P–E loop shapes from the linear capacitor to the ferroelectric capacitor, as well as both the remnant polarization (P_r) and coercive field (E_c), decreased. (The saturation polarization (P_s) of the 45 nm thick film, which is slightly larger than that of the 20 nm thick film, might be due to the slightly higher dielectric loss (but less than 0.1) of the 45 nm thick film than those of the other samples in Fig. 5c.) In particular, the fully strained SMO film (20 nm)

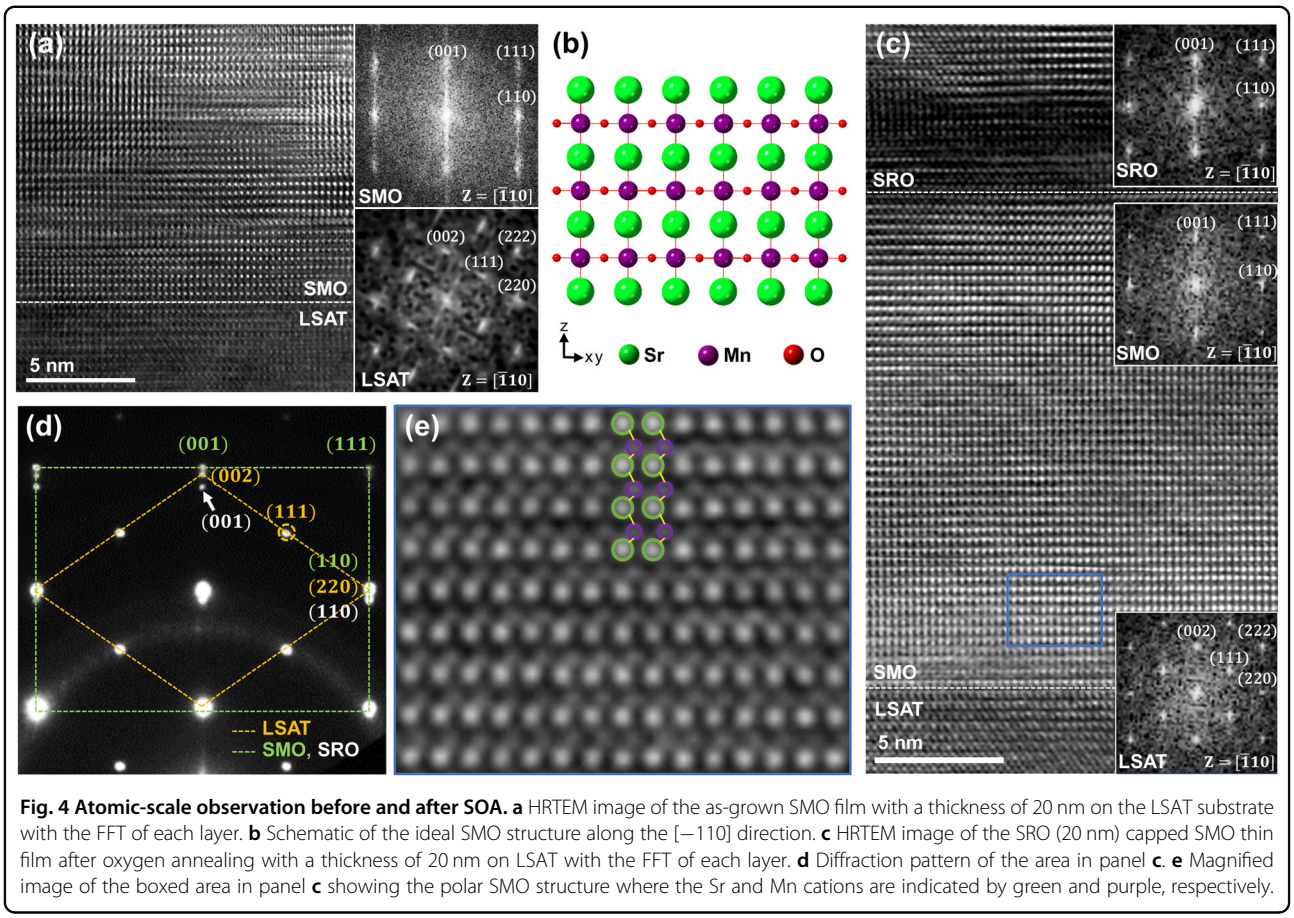

Fig. 4 Atomic-scale observation before and after SOA. a HRTEM image of the as-grown SMO film with a thickness of 20 nm on the LSAT substrate with the FFT of each layer. **b** Schematic of the ideal SMO structure along the [−110] direction. **c** HRTEM image of the SRO (20 nm) capped SMO thin film after oxygen annealing with a thickness of 20 nm on LSAT with the FFT of each layer. **d** Diffraction pattern of the area in panel **c**. **e** Magnified image of the boxed area in panel **c** showing the polar SMO structure where the Sr and Mn cations are indicated by green and purple, respectively.

exhibited a ferroelectric hysteresis loop with a saturation polarization (P_s) of 1 μC/cm^2 and a remnant polarization (P_r) of 0.8 μC/cm^2. Bulk SMO is known as a paraelectric material, and the phase transition to ferroelectric material that appears as an in-plane tensile strain above 1% has been verified through many theoretical[11,15] and experimental results[19,20]. In this regard, we have sufficiently confirmed Mn off-centering of the 1.7% tensile-strained SMO thin film (20 nm) using XRD and HRTEM analysis. Therefore, we believe that such a change in *P*–*E* loop shapes was due to the strain-induced ferroelectricity of SMO.

The measured ε_r for each SMO thin film is shown in Fig. 5c. The ε_r values of the SMO were extracted from the capacitance data using a Gevorgian approximation model, which is suitable for very thin films of 20–115 nm[34–38]. The low dielectric constant of LSAT (ε_r: 22.5)[39] reduces field penetration in the substrate and facilitates modeling of the ε_r of the SMO films when IDEs are used[12,40]. The ε_r results revealed that the strain-relaxed SMO film (115 nm) has a low ε_r (6.7), whereas the fully strained SMO film (20 nm) has a relatively high ε_r (138.1). The low ε_r of the strain-relaxed SMO film is consistent with the paraelectricity of bulk SMO, while it seems that the dielectric constant can be increased by 20 times or more when a tensile strain of 1.7% is applied. Although the dielectric constant of the 1.7% strained SMO thin film is not as high as those observed in $BaTiO_3$[41], $PbTiO_3$[42], and several ferroelectric perovskite oxides found in capacitors, it is comparable to that of typical perovskite multiferroics such as $BiFeO_3$ (BFO)[43]. Additionally, since SMO can optionally become a low-κ or a high-κ material, it can be applied to a wide range of capacitors or memory devices.

In our cases, a significant difference in ε_r arising from the leakage issue is not expected because tan δ of all the thin films is less than 0.1 (right-hand side of Fig. 5c). The thickness dependence of ε_r can be neglected (ε_r increases due to the nonferroelectric dead layer between the film and the electrode when the thickness increases[44–46]) since the current path length of 6 μm is the same for all films, as shown in Fig. S1 (Supplementary information). Moreover, to rule out the effects due to IDE geometry and film thickness dependence, we calculated the dielectric constant using the Gevorgian model. Therefore, we believe that this significant increase in the dielectric constant with decreasing film thickness was due to experimentally identified strain-induced polarization. This indicates that the considerable changes in both the polarization and

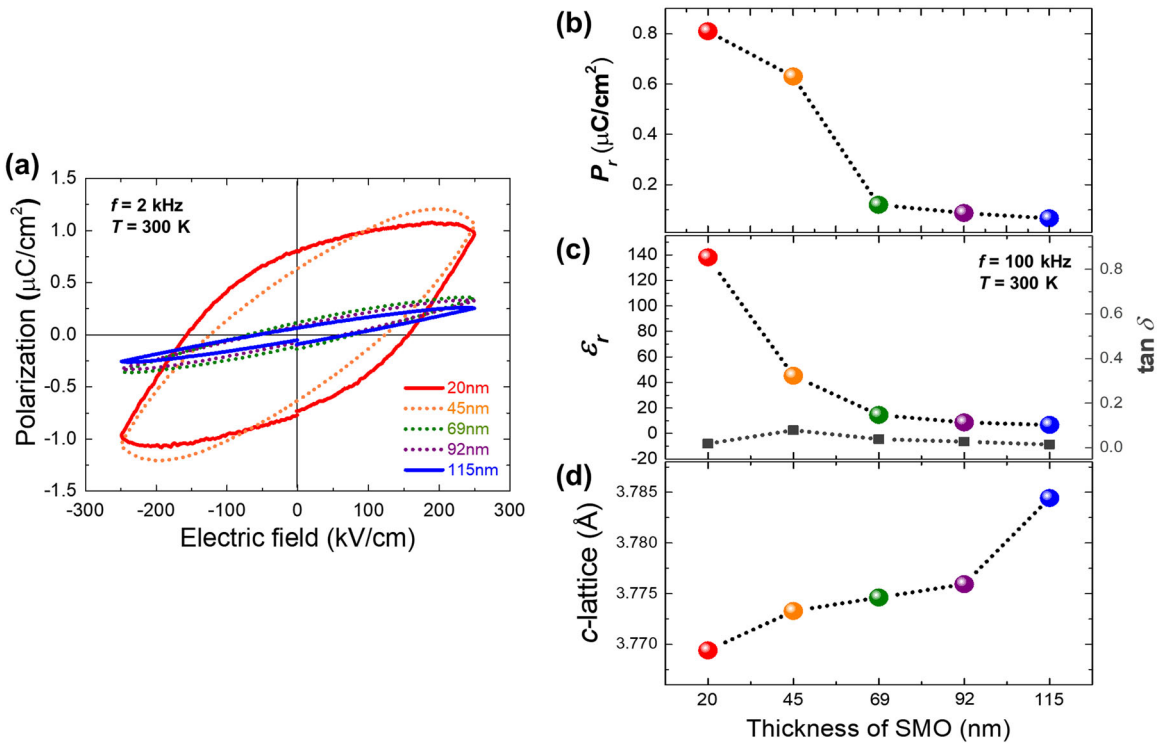

Fig. 5 Strain-induced ferroelectricity at room temperature. a In-plane *P*–*E* loops for the SOA-treated SMO films with thicknesses of 20, 45, 69, 92, and 115 nm at 2 kHz. **b** Remnant polarization values according to the film thickness extracted from the *P*–*E* loops of panel **a**. **c** In-plane dielectric constants ($\varepsilon_r = 138.1$, 45.2, 14.5, 8.7, and 6.7) and dielectric losses (tan $\delta = 0.019$, 0.079, 0.039, 0.028, and 0.015) of the SOA-treated SMO films with thicknesses of 20, 45, 69, 92, and 115 nm, respectively at 100 kHz. **d** Out-of-plane lattice parameters of the SOA-treated SMO films calculated based on the XRD data.

dielectric constant were dominantly affected by strain-induced polar distortion. Consequently, the intrinsic ferroelectric hysteresis loop ($P_s = 1$ μC/cm^2) and dielectric constant ($\varepsilon_r = 138.$ 1) of the 1.7% tensile-strained SMO thin film was experimentally verified for the first time.

Increasing the thickness of the films to control the epitaxial strain enabled observation of the phase transition from paraelectric to ferroelectric SMO. As shown in Fig. 5d, the 20 nm thick SMO film had the most contracted c-lattice parameter, which gradually elongated due to strain relaxation as the thickness increased. Conversely, the remnant polarization (0.81, 0.63, 0.12, 0.09, 0.07) and dielectric constant (138.1, 45.2, 14.5, 8.7, and 6.7) exponentially decreased as the thickness increased, as shown in Figs. 5b, c, respectively. In particular, the gradual increase in the polarization values and dielectric constants when the thickness changed from 115 nm to 69 nm evolved to a rapid increase when the thickness changed from 69 nm to 20 nm. The overall results shown in Fig. 5b–d are consistent with the theoretically calculated diagram, in which the polarization rapidly increases at more than 1% of the epitaxial in-plane strain because of the phase transition from paraelectric to ferroelectric SMO, although the c-lattice parameter gradually decreases[15]. Therefore, the dramatic increase in the dielectric constant when the thickness changed from 45 and 69 nm may be attributed to this phase transition. Finally, we anticipate that a stronger ferroelectric polarization of the SMO thin films accompanying dielectric switching, which was limited in our case due to the large current path length of the in-plane electrodes (Fig. S8 for details), can be realized at room temperature in the near future.

Conclusion

To conclude, we have successfully investigated the intrinsic ferroelectric and dielectric properties of strained SMO thin films using our SOA method. The experimental results confirmed that SOA was able to effectively suppress the high leakage current and air degradation of SMO thin films. Of particular importance is that SOAs not only allow direct investigation of the intrinsic multiferroicity of strained SMO thin films but also allow device applications without leakage issues. Based on their insulating properties, we can determine the ferroelectric polarization loop ($P_s = 1$ μC/cm^2) and the dielectric constant ($\varepsilon_r = 138.1$) of 1.7% tensile-strained SMO thin films. Moreover, the polarization and dielectric constant of the SMO films can be significantly increased from 6.7

to 138.1 via strain engineering. These findings are not only important experimental evidence of strain-induced multiferroic SMO but also a cornerstone for reliably exploring the fundamental physical properties of strained SMO by using the SOA method. We also believe that the experimental realization of the intrinsic strain-induced ferroelectricity of SMO will inspire new avenues for single-phase multiferroics.

Acknowledgements
This research was supported by the Creative Materials Discovery Program (2017M3D1A1040834) through the National Research Foundation of Korea (NRF) funded by the Ministry of Science and ICT.

Author details
[1]School of Materials Science and Engineering, Gwangju Institute of Science and Technology, Gwangju 61005, Republic of Korea. [2]Max Planck POSTECH/Hsinchu Center for Complex Phase Materials & Department of Physics, POSTECH, Pohang 37673, Republic of Korea. [3]School of Advanced Materials and Engineering & Research Center for Advanced Materials Technology, Sungkyunkwan University, Suwon 16419, Republic of Korea. [4]Department of Electrical Engineering, Gachon University, Seongnam 13120, Republic of Korea. [5]Department of Advanced Materials Engineering, Kyonggi University, Suwon, Gyeonggi-do 16227, Republic of Korea. [6]Research Center for Materials Analysis, Korea Basic Science Institute, Daejeon 34133, Republic of Korea

Author contributions
H.A., J.Y. and J.S. fabricated the $SrMnO_3$ thin films. H.A. devised the selective oxygen annealing method and characterized the structural, ferroelectric, and dielectric properties of the grown films. Y.-G.C., Y.-R.J., H.J.H. and B.-J.K. investigated and analyzed the atomic-scale structure of the films using TEM. J.-K.K. and K.-T.K. performed in-depth structural analyses of the films. O.K. and Y.K. performed in-depth ferroelectric analyses of the films. S.K. and C.W.B. fabricated the ceramic targets. Surface morphologies and electric characterizations of the films were carried out by M.S., J.-C.P., H.C., J.L., M.-H.H. and S.R. using a semiconductor parameter analyzer and AFM. S.L. designed and supervised the overall project. H.A., B.-J.K. and S.L. cowrote the manuscript, and all authors commented on the manuscript.

Competing interests
The authors declare no competing interests.

Publisher's note
Springer Nature remains neutral with regard to jurisdictional claims in published maps and institutional affiliations.

Supplementary information The online version contains supplementary material available at https://doi.org/10.1038/s41427-021-00335-7.

Received: 3 March 2021 Revised: 11 August 2021 Accepted: 26 August 2021.
Published online: 29 October 2021

References

1. Hill, N. A. Why are there so few magnetic ferroelectrics? *J. Phys. Chem. B* **104**, 6694–6709 (2000).
2. Martin, L. W. & Ramesh, R. Multiferroic and magnetoelectric heterostructures. *Acta Mater.* **60**, 2449–2470 (2012).
3. Rondinelli, J. M., Eidelson, A. S. & Spaldin, N. A. Non-d^0 Mn-driven ferroelectricity in antiferromagnetic $BaMnO_3$. *Phys. Rev. B* **79**, 205119 (2009).
4. Maurel, L. et al. Nature of antiferromagnetic order in epitaxially strained multiferroic $SrMnO_3$ thin films. *Phys. Rev. B* **92**, 024419 (2015).
5. Kimura, T. et al. Distorted perovskite with e g^1 configuration as a frustrated spin system. *Phys. Rev. B* **68**, 060403 (2003). R.
6. Kimura, T. et al. Magnetic control of ferroelectric polarization. *Nature* **426**, 55–58 (2003).
7. Khomskii, D. Classifying multiferroics: mechanisms and effects. *Physics* **2**, 20 (2009).
8. Ratcliff, W., Lynn, J. W., Kiryukhin, V., Jain, P. & Fitzsimmons, M. R. Magnetic structures and dynamics of multiferroic systems obtained with neutron scattering. *npj Quantum Mater.* **1**, 16003 (2016).
9. Agrawal, P. et al. Strain-driven oxygen deficiency in multiferroic $SrMnO_3$ thin films. *Phys. Rev. B* **94**, 104101 (2016).
10. Ramesh, R. & Spaldin, N. A. Multiferroics: progress and prospects in thin films. *Nat. Mater.* **6**, 21–29 (2007).
11. Edström, A. & Ederer, C. First-principles-based strain and temperature-dependent ferroic phase diagram of $SrMnO_3$. *Phys. Rev. Mater.* **2**, 104409 (2018).
12. Haeni, J. H. et al. Room-temperature ferroelectricity in strained $SrTiO_3$. *Nature* **430**, 758–761 (2004).
13. Antons, A., Neaton, J. B., Rabe, K. M. & Vanderbilt, D. Tunability of the dielectric response of epitaxially strained $SrTiO_3$ from first principles. *Phys. Rev. B* **71**, 024102 (2005).
14. Eklund, C., Fennie, C. J. & Rabe, K. M. Strain-induced ferroelectricity in orthorhombic $CaTiO_3$ from first principles. *Phys. Rev. B* **79**, 220101 (2009). R.
15. Lee, J. H. & Rabe, K. M. Epitaxial-strain-induced multiferroicity in $SrMnO_3$ from first principles. *Phys. Rev. Lett.* **104**, 207204 (2010).
16. Lee, J. H. et al. A strong ferroelectric ferromagnet created by means of spin-lattice coupling. *Nature* **466**, 954–958 (2010).
17. Fennie, C. J. & Rabe, K. M. Magnetic and electric phase control in epitaxial $EuTiO_3$ from first principles. *Phys. Rev. Lett.* **97**, 267602 (2006).
18. Hong, J., Stroppa, A., Íñiguez, J., Picozzi, S. & Vanderbilt, D. Spin-phonon coupling effects in transition-metal perovskites: A DFT + U and hybrid-functional study. *Phys. Rev. B* **85**, 054417 (2012).
19. Becher, C. et al. Strain-induced coupling of electrical polarization and structural defects in $SrMnO_3$ films. *Nat. Nanotechnol.* **10**, 661–665 (2015).
20. Guzmán, R. et al. Polar-graded multiferroic $SrMnO_3$ thin films. *Nano Lett.* **16**, 2221–2227 (2016).
21. Wang, H. et al. Direct observation of huge flexoelectric polarization around crack tips. *Nano Lett.* **20**, 88–94 (2020).
22. Guo, J. W. et al. Strain-induced ferroelectricity and spin-lattice coupling in $SrMnO_3$ thin films. *Phys. Rev. B* **97**, 235135 (2018).
23. You, J. et al. Moisture assisted perovskite film growth for high performance solar cells. *Appl. Phys. Lett.* **105**, 183902 (2014).
24. Noh, J. H. et al. Chemical management for colorful, efficient, and stable inorganic–organic hybrid nanostructured solar cells. *Nano Lett.* **13**, 1764–1769 (2013).
25. Mamun, A. A., Mohammed, Y., Ava, T. T., Namkoong, G. & Elmustafa, A. A. Influence of air degradation on morphology, crystal size and mechanical hardness of perovskite film. *Mater. Lett.* **229**, 167–170 (2018).
26. Islamov, D. R. et al. Identification of the nature of traps involved in the field cycling of $Hf_{0.5}Zr_{0.5}O_2$-based ferroelectric thin films. *Acta Mater.* **166**, 47–55 (2019).
27. Weber, D., Vőfély, R., Chen, Y., Mourzina, Y. & Poppe, U. Variable resistor made by repeated steps of epitaxial deposition and lithographic structuring of oxide layers by using wet chemical etchants. *Thin Solid Films* **533**, 43–47 (2013).
28. Vorobiev, A. & Gevorgian, S. Intrinsically switchable thin film bulk acoustic wave resonators. *Appl. Phys. Lett.* **104**, 222905 (2014).
29. Cai, W. et al. Significant performance improvement of oxide thin-film transistors by a self-assembled monolayer treatment. *Adv. Electron. Mater.* **6**, 1901421 (2020).
30. Lien, C. et al. The demonstration of high-performance multilayer $BaTiO_3$/$BiFeO_3$ stack MIM capacitors. *IEEE Trans. Electron Devices* **65**, 4834–4838 (2018).
31. Lee, B. H. et al. Issues with the electrical characterization of graphene devices. *Carbon Lett.* **13**, 23 (2012).
32. Seo, S., Kang, H., Jang, H. & Noh, D. Effects of oxygen incorporation in tensile $La_{0.84}Sr_{0.16}MnO_{3-\delta}$ thin films during ex situ annealing. *Phys. Rev. B* **71**, 012412 (2005).
33. Park, K. W. et al. Observation and tunability of room temperature photoluminescence of GaAs/GaInAs core-multiple-quantum-well shell nanowire structure grown on Si (100) by molecular beam epitaxy. *Nanoscale Res. Lett.* **9**, 626–636 (2014).
34. Gevorgian, S. S., Martinsson, T., Linner, P. L. & Kollberg, E. L. CAD models for multilayered substrate interdigital capacitors. *IEEE Trans. Microw. Theory Tech.* **44**, 896–904 (1996).
35. Chidambaram, N., Mazzalai, A., Balma, D. & Muralt, P. Comparison of lead zirconate titanate thin films for microelectromechanical energy harvester with interdigitated and parallel plate electrodes. *IEEE Trans. Ultrason. Ferroelectr. Freq. Control* **60**, 1564–1571 (2013).

36. Folkman, C. et al. Study of defect-dipoles in an epitaxial ferroelectric thin film. *Appl. Phys. Lett.* **96**, 052903 (2010).
37. Folkman, C. M. Spontaneous strain and ferroelectric-ferroelastic behavior in epitaxial bismuth ferrite thin films. The University of Wisconsin - Madison. ProQuest Dissertations Publishing, 3437001 (2010).
38. Kidner, N., Homrighaus, Z., Mason, T. O. & Garboczi, E. Modeling interdigital electrode structures for the dielectric characterization of electroceramic thin films. *Thin Solid Films* **496**, 539–545 (2006).
39. Tidrow, S. et al. New substrates for HTSC microwave devices. *IEEE Trans. Appl. Supercond.* **7**, 1766–1768 (1997).
40. Canedy, C. et al. Dielectric properties in heteroepitaxial $Ba_{0.6}Sr_{0.4}TiO_3$ thin films: effect of internal stresses and dislocation-type defects. *Appl. Phys. Lett.* **77**, 1695–1697 (2000).
41. Lee, H. N., Christen, H. M., Chisholm, M. F., Rouleau, C. M. & Lowndes, D. H. Strong polarization enhancement in asymmetric three-component ferroelectric superlattices. *Nature* **433**, 395–399 (2005).
42. He, B. & Wang, Z. Enhancement of the electrical properties in $BaTiO_3$/$PbZr_{0.52}Ti_{0.48}O_3$ ferroelectric superlattices. *ACS Appl. Mater. Interfaces* **8**, 6736–6742 (2016).
43. Song, J. et al. Enhancement of ferroelectric properties of superlattice-based epitaxial $BiFeO_3$ thin films via substitutional doping effect. *J. Phys. Chem. C* **123**, 11564–11571 (2019).
44. Pintilie, L., Vrejoiu, I., Hesse, D., Le Rhun, G. & Alexe, M. Extrinsic contributions to the apparent thickness dependence of the dielectric constant in epitaxial Pb(Zr, Ti)O_3 thin films. *Phys. Rev. B* **75**, 224113 (2007).
45. Zhou, X. Y. et al. Thickness dependence of in-plane dielectric and ferroelectric properties of $Ba_{0.7}Sr_{0.3}TiO_3$ thin films epitaxially grown on $LaAlO_3$. *Appl. Phys. Lett.* **90**, 132902 (2007).
46. Yang, Q., Cao, J., Zhou, Y., Sun, L. & Lou, X. Dead layer effect and its elimination in ferroelectric thin film with oxide electrodes. *Acta Mater.* **112**, 216–223 (2016).